Available online at www.sciencedirect.com

ScienceDirect

Ceramics International 40 (2014) 4879–4887

CERAMICS INTERNATIONAL

www.elsevier.com/locate/ceramint

Thermal cycle development of PMMA pore former removal for honeycomb-type SOFC supports

Seung Jin Lee[a], Jeong Myeong Lee[a], Yoon Gon Kim[a], Soon Do Yoon[b], Jeong Woo Yun[a,*]

[a]School of Applied Chemical Engineering, Chonnam National University, Gwangju 500-757, Republic of Korea
[b]Department of Chemical and Biomolecular Engineering, Chonnam National University, Yeosu 550-749, Republic of Korea

Received 17 June 2013; received in revised form 26 August 2013; accepted 10 September 2013
Available online 16 September 2013

Abstract

Heating schedules of polymethyl methacrylate (PMMA) pore former removal are developed to fabricate anode-supported, honeycomb-type, solid oxide fuel cells (SOFCs) without any defects. The cycles are determined for the thermal removal of polymeric pore former and binder from open-pore, green ceramic components. The samples consist of a honeycomb-shaped green body composed of Ni/YSZ as the anode support, PMMA beads as the pore former, and methylcellulose as the binder. The kinetic parameters of the PMMA decomposition, the gas permeability in the body, and the failure conditions during heating are determined both experimentally and by modeling. The results of these measurements and approximations are incorporated into a variational calculus algorithm for predicting the minimum time heating cycle (MTHC).

Keywords: Honeycomb type; Solid oxide fuel cells; Anode support; Heating cycle; Kinetics

1. Introduction

Solid oxide fuel cells (SOFCs) have been studied as a promising energy conversion system due to their high energy efficiency and low emission. So far, two main types of SOFCs have been developed: bipolar planar and tubular. Although planar-type SOFC stacks have relatively high power densities per volume and low capital coats, considerable technical barriers, such as a gas sealing and interconnection materials, remain before their commercial application is assured. Tubular-type SOFC stacks, on the other hand, have technical advantages compared to the planar-type SOFC stacks, such as technical simplicity and reliability, including sealing problems. The low power densities per volume and high manufacturing costs, however, remain as major disadvantages for tubular-type SOFC stacks. Recently, to overcome the barriers in these two types, various new types, such as the so-called honeycomb-type SOFCs, have been attracting much interest [1]. The ideal honeycomb-type SOFCs would combine the low fabrication cost and high power densities of the planar-type SOFCs with the simplicity and reliability of the tubular-type SOFCs, while still offering sufficient mechanical strength. Wetzko et al. successfully produced the first honeycomb-type SOFCs using yttria-stabilized zirconia (YSZ) electrolyte [2]. They reported a power density for 5 honeycomb stacks of 120 mW/cm^2 at 1000 °C. They concluded that the operating temperature should be decreased and the stack performance decreased for long-term operation due to gas sealing and interconnection problems. Zhong et al. studied honeycomb-type SOFCs with $La_{0.9}Sr_{0.1}Ga_{0.8}Mg_{0.2}O_3$ (LSGM) electrolyte for reducing the temperature and production costs [3]. They reported a power density of 250 mW/cm^2 in a single channel at 800 °C, even under gas leakage conditions. Electrolyte honeycomb-supported SOFCs, however, suffer the essential weakness of a high ohmic resistance due to the thick electrolyte. Yamaguchi et al. studied cathode-honeycomb-supported SOFCs using $LaSrMnO_3$ (LSM) [4,5]. They reported a power density of 48 mW/cm^2 and 81 mW/cm^2 at 600 °C and 650 °C, respectively, with a thin scandia-stabilized electrolyte. Electrode-supported types should be superior to electrolyte-supported types due to the thin electrolyte layer leading to low electrolyte resistance and the entire exclusive channels for air or fuel when the porous honeycomb electrode is used. However, fabricating

*Corresponding author. Tel.: +82 62 530 1908; fax: +82 62 530 1889.
E-mail address: jwyun@jnu.ac.kr (J. W. Yun).

0272-8842/$ - see front matter © 2013 Elsevier Ltd and Techna Group S.r.l. All rights reserved.
http://dx.doi.org/10.1016/j.ceramint.2013.09.040

the porous electrode honeycomb support and coating the thin electrolyte layer on the highly porous honeycomb channel surface may be a much more difficult and expensive process due to the requirement for a defect-free body with homogeneous density which affects the cracking in the honeycomb wall and the subsequent structural failure during the sintering process at high temperature over 1300 °C.

To introduce the gas path through the pore in the ceramic honeycomb, a polymeric pore former, typically polymethyl methacrylate (PMMA), was uniformly mixed with the anode powder, binder and some additives in the solvent. The loss of the pore former and the binder by heating is expected to both increase the porosity and change the surface area to volume ratio within the porous honeycomb. Both these effects will affect the permeability and hence the mass transfer of gas to electrochemical active site. Thermal decomposition of the pore former and the binder may lead to conversion of the solid state to gas phase products. Excessive pressure associated with the decomposition products may introduce defects into the ceramic body or induce fracture of the ceramic honeycomb. To avoid such failures through the honeycomb support, slow heating cycles with multiple hold periods are necessary, which necessitate that the heat treatment time for thermal removal of the pore former and the binder can be the single longest processing operation and hence result in a total duration of hundreds of hours. Therefore, the heat treatment schedules for the pore former and binder become important so as to maximize the yield while minimizing the furnace time and ensuring a defect-free body.

In our earlier works [6–8], we developed an algorithm for determining the minimum time heating cycle (MTHC) for polymeric binder removal from open-pore, green ceramic bodies in which convection is the dominant flow by which the products of binder decomposition exit the ceramic body. Although a few of the parameters and values regarding the failure pressure and failure stress during heating cycles have been reported or remain unknown because of the complexity of the coupling between mass transfer, reaction kinetics, and failure analysis, the study results were acceptable. We successfully fabricated defect-free ceramic bodies using the MTHC schedule.

In the present work, aimed at fabricating anode-supported honeycomb-type SOFCs without any defects that typically arise during thermal pore former removals, we applied the previously developed algorithm to the new honeycomb substrate. Several parameters appearing in such heating cycles were specified, including the decomposition kinetics, permeability, porosity, scaling and distribution of the pore former, and other conditions during heat treatment. Failure pictures of the fabricated honeycomb supports with a linear ramping rate of 1 °C/min are shown in Fig. 1. The honeycomb support has 9 channels (4 channels for fuel and the other 5 channels for air/O_2). Moreover, we coated the 8YSZ as an electrolyte on the porous honeycomb wall surface in dip-coating method, after which the LSM cathode was coated on the electrolyte in tape-casting method. The single cell and stack performance of the honeycomb-type SOFCs will be discussed later.

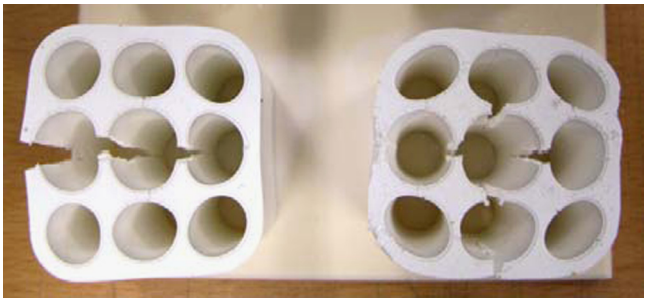

Fig. 1. Failure images of the honeycomb supporter.

2. Experimental

A mixture of 50 wt% NiO and 50 wt% 8YSZ was mixed to prepare the anode honeycomb support. The NiO/YSZ slurry was prepared by mixing with PMMA beads as the fore former, methyl cellulose as the binder, and additives in water. The NiO/YSZ powder containing the pore former was prepared by spray drying in air. The honeycomb support with 9 channels was prepared from uniaxial pressurization of the spray-dried power. The dimensions of the honeycomb support were 36 mm high and 43 mm wide, with a channel diameter of 11 mm. To determine the appropriate porosity and pore diameter with sufficient strength for several honeycomb stacks, 3 different sizes of PMMA beads (5, 12 and 30 μm) mixed with the NiO/YSZ power were analyzed. The porosity and pore diameter were analyzed for various amounts of pore former with a mercury intrusion porosimeter. The kinetic parameters of polymeric material decomposition in the green honeycomb cell, such as pre-exponential factors, A, and activation energies, E, were obtained from thermogravimetric analysis (TGA) in 60 cm^3/min air flowing at different linear heating rates. After removing the organic materials, the honeycomb supports were sintered at 1480 °C for 2 h. The dimensions of the final honeycomb supports were 28 mm high and 31 mm wide, with a channel diameter of 7.5 mm. The YSZ slurry for the dense electrolyte was prepared by mixing a commercial 8 mol% Y_2O_3–ZrO_2 powder(TZ-8YSZ, Tosoh) with PVB (poly vinyl butyral, Butvar B98 Richard E. Mistler Inc.), DBP (dibutyl phthalate), and other additives in Toluene/IPA solvent at room temperature. A thin YSZ electrolyte layer with thickness of 20 μm was formed on the wall surface of the porous honeycomb support by dip-coating method and then sintered at 1500 °C for 2 h with a ramping rate of 5 °C/min. The $LaSrMnO_3$ slurry as a cathode material prepared by mixing with PVB, DBP, and additives in solvents was coated on the electrolyte in the dip-coating method and then sintered at 1100 °C for 2 h. To connect the current path between the honeycomb stacks, an appropriate area in the honeycomb support was masked before applying the twin processes of electrolyte and cathode coating. A schematic concept of the anode-supported honeycomb SOFC stacks is illustrated in Fig. 2.

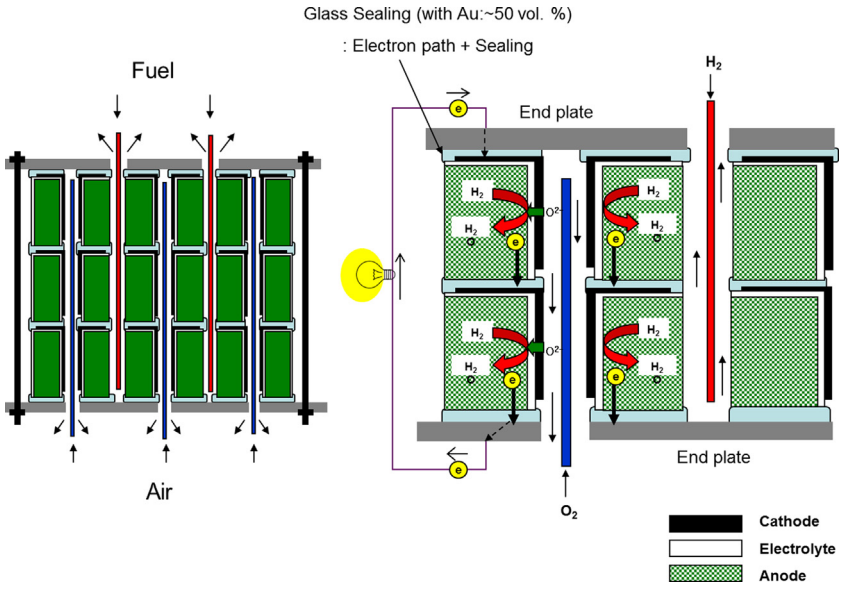

Fig. 2. Schematic concept of the anode-supported honeycomb SOFC stacks.

3. Model

The governing equations and models for the thermal degradation of the polymer have been derived elsewhere [6,8], and so we simply summarize herein the main results. The rate of polymeric pore former and binder decompositions, r, is given by,

$$\mathrm{r} = -\frac{\mathrm{da}}{\mathrm{dt}} = \mathrm{Aexp}\left(-\frac{\mathrm{E}}{\mathrm{RT}}\right) f(a) \tag{1}$$

where a represents the weight of polymer, and A and E represent the pre-exponential factor and activation energy, respectively. We have developed several different kinetic mechanisms for the thermal degradation [6]. The first-order decomposition kinetics in which $f(a)$ is $(1\text{-}a)$ were assumed in this study. A and E obtained from TGA experiments with linear heating rate, β, can be obtained by Lee and Beck's model [9] from

$$\ln\left[\frac{-\ln(1-a)}{T^2}\right] = \ln\left[\frac{AR}{\beta(E+2RT)}\right] - \frac{E}{RT} \tag{2}$$

as described in more detail elsewhere [6,8]. The permeability in the green body, κ, can be determined by the Kozeny–Carmen equation as,

$$\kappa = \frac{\varepsilon^3}{k(1-\varepsilon)^2 S^2} \tag{3}$$

where ε is the porosity, k a geometrical constant and S the specific surface. The volume fraction of porosity ε is related to ε_p and the volume fraction of solids ε_s as

$$\varepsilon = 1-\varepsilon_s-\varepsilon_p \tag{4}$$

The gas permeability can be assumed isotropic in any direction when the pore former and ceramics are dispersed uniformly. The pressure distribution in a three-dimensional porous medium of parallelepiped geometry from the thermal decomposition of polymeric pore former was obtained under the following assumptions: (i) a uniform temperature in the body, (ii) a constant viscosity, μ, of the decomposition products, and (iii) constant dimensions of the sample during heating the sample. The process for the pressure distribution in porous medium, which is described with non-linear, 3D and unsteady state partial differential equations, was derived by an analytical solution in the form of a Fourier series under the assumption of a pseudo-steady state. Only the leading term is then used to describe the pressure distribution; the accuracy of this assumption has been discussed elsewhere [10,11]. With the above assumptions, the normalized internal pressure, $(P/P_o)_o$, occurring in the center of the body during decomposition of the pore former is given by

$$\left(\frac{P}{P_o}\right)_o \approx \left(1+G\frac{rT}{\kappa}\right)^{1/2} \tag{5}$$

Eq. 5 thus describes the pressure in the center of the body in terms of reaction rate, r, permeability, k, temperature, T, and another constant, G. Then, the constant G in Eq. 5 is given by

$$G = 0.8365\frac{\mu\rho_b}{2\rho_o^2 RMT_o^2}\frac{L_x^2L_y^2L_z^2}{L_x^2L_y^2+L_y^2L_z^2+L_x^2L_z^2} \tag{6}$$

To obtain the heating schedule of the ceramic green body, a temperature versus time function should be determined without exceeding a failure stress that is proportional with the pressure in the center of the green body. The time depending on the volume fraction of the pore former from initial pore former loading, ε_{po}, to any remaining loading is expressed and obtained by variational calculus as [11]

$$\mathrm{t} = \frac{\mathrm{GT}_s}{\mathrm{P}_t^2-1}\int_{\varepsilon_p}^{\varepsilon_{po}}\frac{d\varepsilon_p}{\kappa(\varepsilon_P)}$$

$$= \frac{GT_skS^2}{P_t^2-1}\times\left[\frac{1}{3}\left\{\frac{1}{(1-\varepsilon_s-\varepsilon_{Po})^3}-\frac{1}{(1-\varepsilon_s-\varepsilon_P)^3}\right\}-\right.$$

$$\left\{\frac{1}{(1-\varepsilon_s-\varepsilon_{Po})^2}-\frac{1}{(1-\varepsilon_s-\varepsilon_P)^2}\right\}+\left\{\frac{1}{(1-\varepsilon_s-\varepsilon_{Po})}-\frac{1}{(1-\varepsilon_s-\varepsilon_p)}\right\}\Bigg] \quad (7)$$

where T_s is the starting temperature and P_t, the threshold pressure, is the value of $(P/P_o)_o$ in Eq. 5 corresponding to when failure in the body occurs. Eq. (7) can thus represent the time schedule for pore former removal corresponding to the development of the pore or removal of the pore former in volume fraction. Although the time in Eq. (7) does not explicitly depend on the decomposition kinetics via A and E, the temperature of the pore former removal does depend on the kinetics as given by [11]

$$T=-\frac{E}{R}\left[\ln\frac{\kappa(P_t^2-1)}{\varepsilon_b G T_s A}\right]^{-1} \quad (8)$$

Eqs. (7) and (8) are thus the primary expressions used to specify the minimum heating schedule of the polymeric pore former without any defects in the body. The quantities appearing in the constant G, therefore, must be known, as well as the kinetic parameters, the permeability and the threshold pressure.

4. Results and discussion

The parameters required for developing the heating schedule model are summarized in Table 1. The decomposition gas by oxidation was assumed to be mainly CO_2 and thus the viscosity and molecular weight were taken from those of CO_2. To obtain the kinetic parameters, E and A, during the pore former and binder decomposition, a TGA experiment was conducted at different heating rates in air, and mixing with YSZ and Ni/YSZ. The kinetic parameters shown in Table 2, along with the regression coefficients and the range of conversion evaluated, were obtained from Eq. 3. For the four heating rates of 3YSZ with PMMA beads, the values of A and E were similar, which suggests that the mechanisms of decomposition were invariant over the range of heating rates examined here. Fig. 3 shows the decomposition behaviors of the pore former and the binder in the presence of YSZ, and the predicted kinetics at each heating rate for the first-order decomposition mechanism. The samples were prepared by uniaxial pressurization under 1 MPa and heated at given heating rates, as shown in Fig. 3. The speed of weight loss for all heating rates increased rapidly at 210 °C, and the reactions were mostly completed at 400 °C. As the heating rate was increased, the weight loss profiles were shifted to higher temperatures and the region of rapid polymer degradation seemed to be a function of the heating rate. Fig. 4 shows the kinetic behaviors of the different composition mixtures with the pure PMMA, the YSZ with PMMA, and the Ni/YSZ with PMMA. The decomposition behaviors of the different mixtures were acquired at a heating rate in air of 2 °C/min. For the Ni/YSZ, 50 vol% YSZ or 50 vol% Ni/YSZ (70 wt% NiO and 30 wt% 8YSZ) was mixed with pure PMMA beads. In the presence of PMMA beads with YSZ, the degradation profile was shifted to a higher temperature compared to that of the pure PMMA beads, because the YSZ ceramic power blocked the pathway of the decomposed gas product from the center of the body. The PMMA with Ni/YSZ mixture, however, was degraded at a lower temperature compared to the mixture of PMMA and YSZ power due to the catalytic effects of the nickel.

Gas transport from the anode channel to the electrolyte layer necessitates sufficient pore size and porosity in the honeycomb body. We analyzed three different sizes of PMMA bead as a pore former, as shown in the images of Fig. 5 all at the same magnification: 5 μm (a) and 12 μm (b) and 30 μm (c). The pore diameter in Fig. 6(a) and porosity in Fig. 6(b) using the Ni/YSZ and PMMA mixtures were analyzed for various sizes of PMMA bead as a function of the PMMA volume fractions with a mercury porosimeter. The samples were prepared by uniaxial dry pressing of the mixture power and sintered at 1500 °C for 2 h after removing the PMMA beads at 700 °C in air. The pore diameters and porosities were increased with increasing diameter of the PMMA beads and volume fraction of the PMMA beads. For a PMMA bead size of 30 μm, the pore diameter was over 8.7 μm and the porosity was over 47% after sintering in the 60 vol% PMMA. Otherwise, for a PMMA bead size of 5 μm, the pore diameter was 1.5 μm and the porosity was 37% after sintering. Improved gaseous phase

Table 1
Experimental parameters.

P_0	10,0000	Pa
T_0	300	K
M	44	g/mol
R	8.314	$m^3Pa/mol \cdot K$
μ	0.000025	Pa
S	6×10^6	m^{-1}
k	5	(–)
ρ_b	1000	kg/m^3
ε_s	0.3	(–)
ε_{bo}	0.5	(–)
ε	0.2	(–)
sL_x	0.02	m
L_y	0.02	m
L_z	0.02	m

Table 2
Kinetic parameters and regression coefficients from the first-order decomposition kinetics at different heating rates.

Materials (–)	β (°C/min)	E_a (kJ/mol)	A (s^{-1})	R^2 (–)	$1-\alpha$ (–)
3YSZ with PMMA	1	71.4	721	0.99	0.99–0.01
	2	70.6	1046	0.99	0.99–0.01
	5	68.6	1178	0.99	0.98–0.05
	10	71.8	4158	0.99	0.98–0.01
Pure PMMA	2	128.1	2.48×10^9	0.96	0.98–0.11
Ni/YSZ with PMMA	2	97.9	1.37×10^6	0.97	0.99–0.31

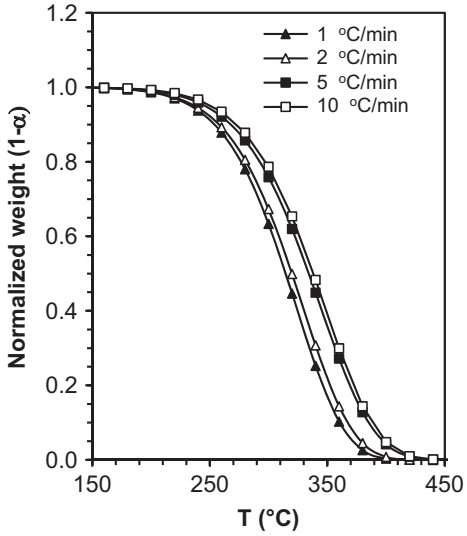

Fig. 3. Thermogravimetric weight loss data heated at different heating rates of 1, 2, 5, 10 °C/min and the kinetics predicted by first-order decomposition mechanisms.

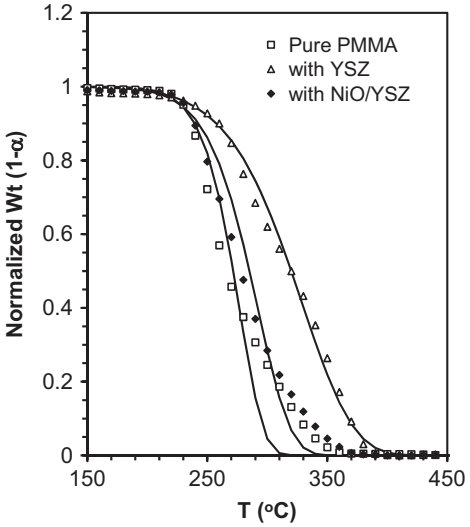

Fig. 4. Thermogravimetric weight loss data heated at 2 °C/min for various anode compositions with pure PMMA, PMMA with 3YSZ, and PMMA with NiO/8YSZ, and the predicted decomposition behavior in the analyzed kinetic parameters shown in table 2.

diffusion in the anode substrate necessitates larger pore diameter and porosity. The mechanical strength of the samples, however, was significantly decreased by over 50% in porosity and the resulting sample would be too brittle, which is not appropriate for the honeycomb supports. Fig. 7 shows the sample images after sintering of 65% (a) and 47% (b) porosities from the PMMA bead size of 30 μm in Ni/YSZ. Therefore, to fabricate the honeycomb type anode support with sufficient strength and appropriate gas permeability, 60 vol% PMMA beads of size 30 μm were used in this study. The average porosity, average pore size and density of this sample were 46.9%, 8.7 μm, and 2.8 g/cm^3, respectively. The cross sectional images are shown in Fig. 8 for low (a) and high (b)

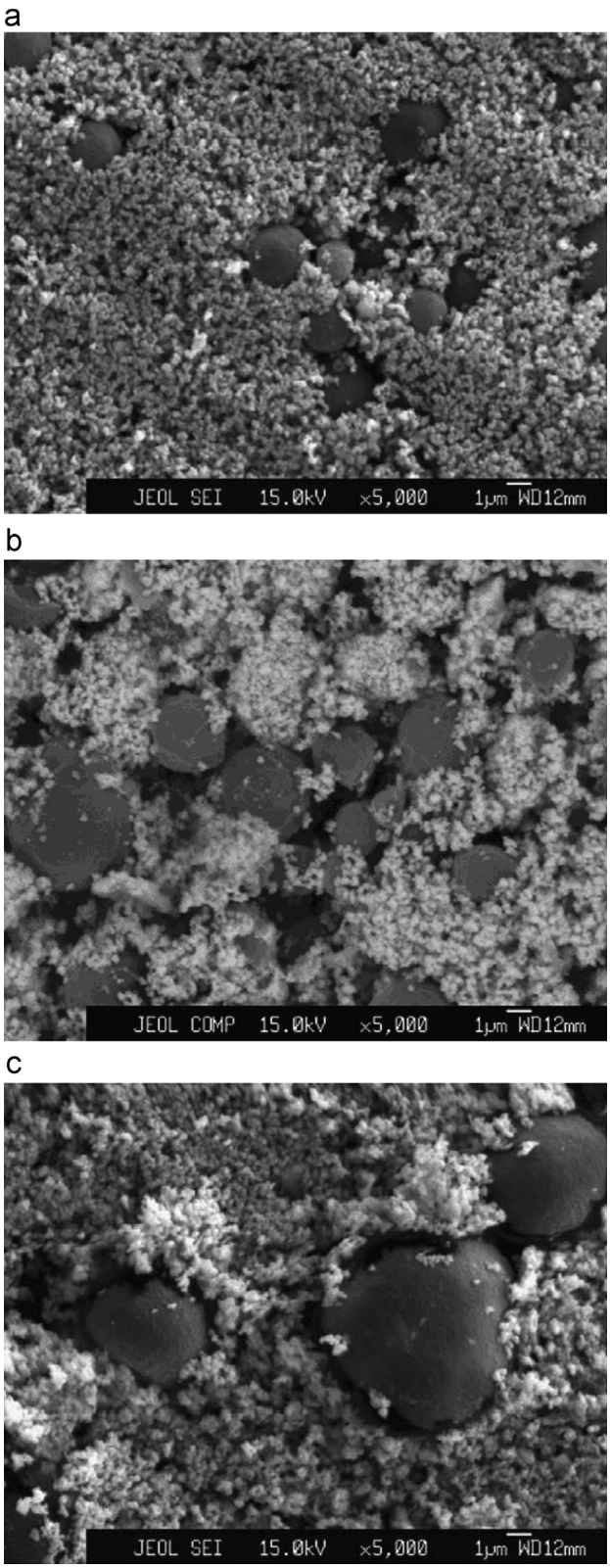

Fig. 5. Scanning electron microscopy images before sintering of Ni/YSZ anode with 5 μm, 12 μm, and 30 μm PMMA pore former beads.

magnification images. The pores for gas permeability were well developed without any significant cracks or fractures.

During heating cycles for pore former and binder removal, the decomposition of the pore former and binder induces

pressure within the sample body and, depending on the kinetics of decomposition, possibly failure of the body. One important input to the model is thus the threshold pressure, P_t, which corresponds to the pressure in the center of the body at failure. To the best of our knowledge, no method has been reported for measuring the failure pressure within a porous body. To circumvent this difficulty, we have developed the following procedure to obtain a value for P_t. Components of parallelepiped geometry are subjected to rapid linear heating rates. During the course of the rapid heating cycle, we visually monitor the sample and record the temperature, T_f, at which failure occurs. To determine P_t, we then use Eqs. (3), (4), (5), and (6) with the known heating rate and calculate $(P/P_o)_o$ as a function of temperature. In performing this calculation, however, we need to assume a decomposition mechanism with associated values of A and E. Fig. 7 shows the results of this type of calculation for the pressure in the center of the body as a function of temperature when components of cube geometry are heated with varying linear heating rates of 1, 2, 5 and 10 °C/min (a) and varying cube geometries at a linear heating rate of 1 °C/min (b). With increasing temperature, the rate of decomposition increases, and thus the pressure increases to a maximum as the pore former and the binder are consumed and the body becomes more permeable. The pressure subsequently decreases as the pore former and binder are consumed and the pore spaces open up. The model parameters used for these simulations are presented in Table 2, along with the kinetic parameters. These parameters were obtained by simulating the TGA data with a first-order mechanism at various heating rates and various sample sizes. We can also determine the threshold pressure, P_t, from the values of $(P/P_o)_o$ indicated in Fig. 9, corresponding to the observed failure temperature, T_f. In the case of one failure pressure, a second temperature exists to the right of the maximum in pressure at which failure may occur. Obviously, if a body fails at the lower temperature, then the second failure temperature is not meaningful. This example does indicate that if a green sample body can survive failure at low temperature for a specific pressure, where the body is full of the binder and relatively strong, then it may still fail later in the heating cycle, when the green body contains less binder and hence is weaker. The above procedure indicates how observation of T_f can be used, with an assumed kinetic model, to determine P_t. To determine the failure temperature, the green samples were heated at linear heating rates under visual monitoring, and the temperature range was recorded during the period of failure. The failure temperatures were observed at a heating rate of 1 °C/min. Although it was difficult to precisely ascertain when the failure occurs, the sample started to crack within a 40 °C temperature window from approximately 170–210 °C. The observance of large macroscopic defects such as bloating and cracking does not preclude the occurrence of

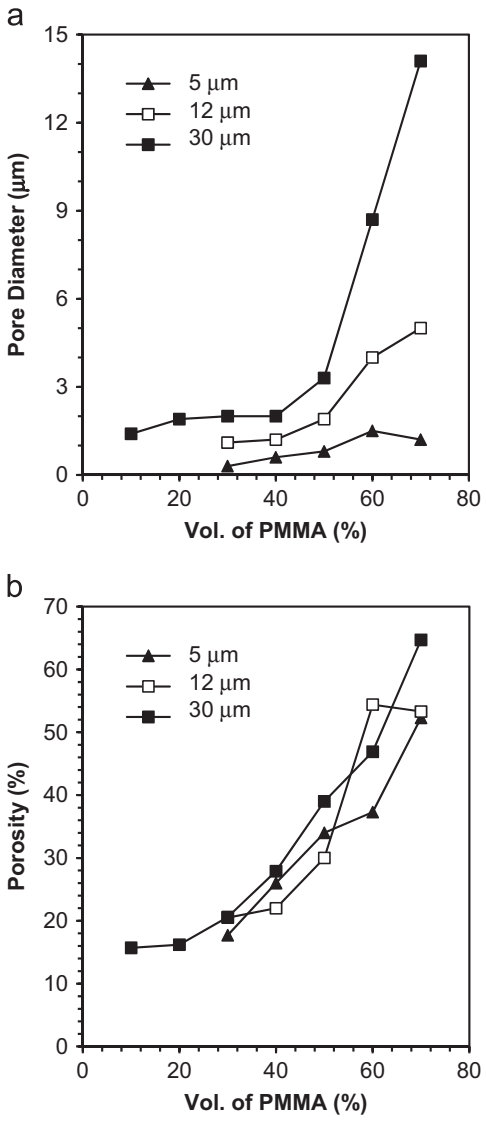

Fig. 6. Pore size (a) and porosity (b) analysis for various volume percentages of PMMA pore former for different sizes of pore formers (5, 12 and 30 μm).

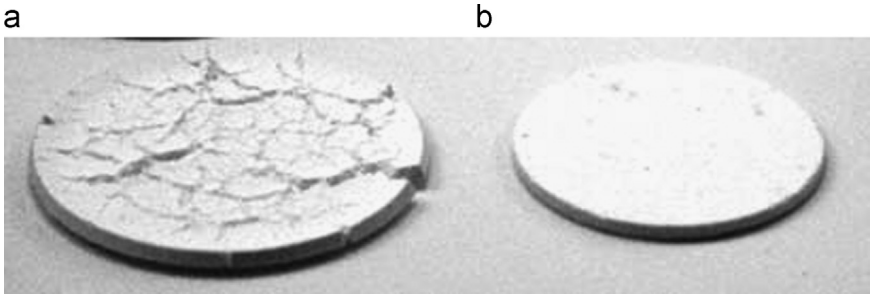

Fig. 7. Button cell images after sintering for a cracked cell with 65 vol% porosity and a successful cell with 47 vol% porosity.

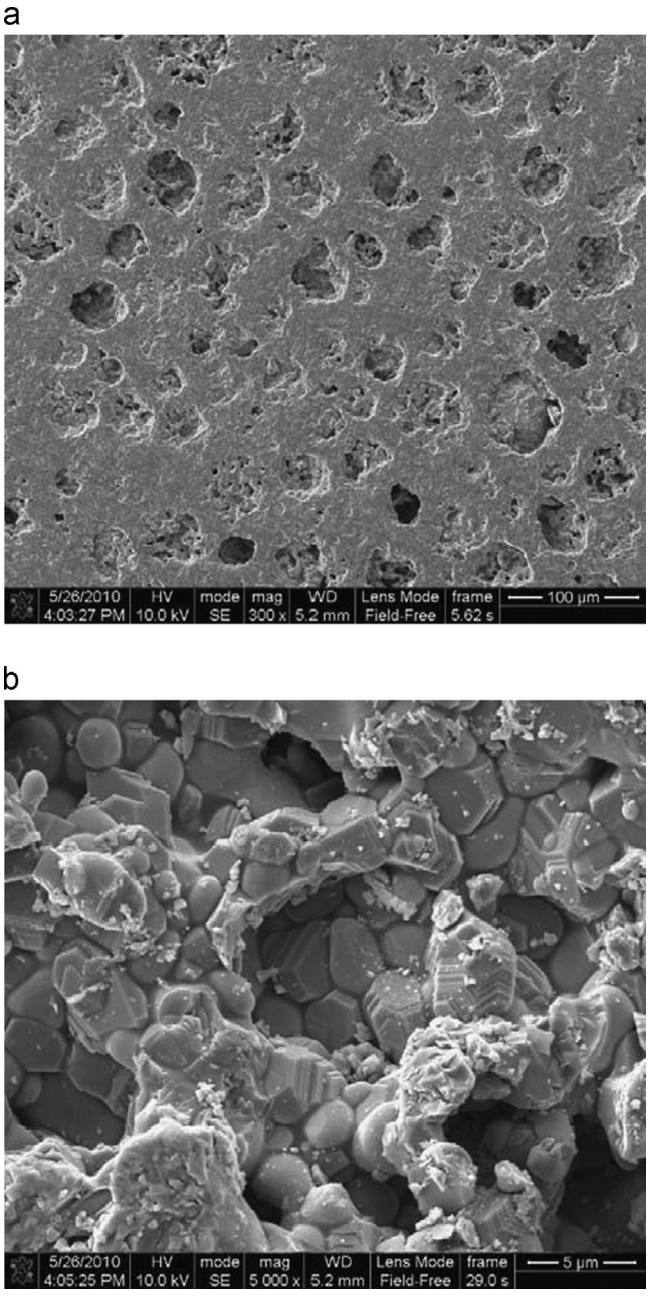

Fig. 8. Scanning electron microscopy images of 60 vol% PMMA beads of size 30 µm for low (a) and high (b) magnification images.

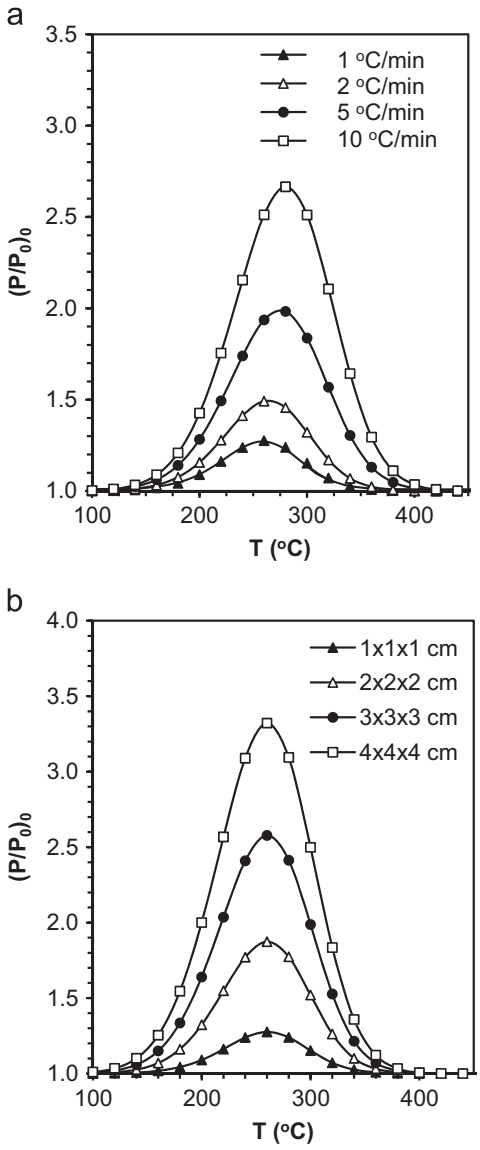

Fig. 9. Normalized pressure in the center of the body, $(P/P_o)_o$, versus temperature for various PMMA bead sizes for the first-order decomposition kinetics at various heating rates (a) and for various sample sizes with 1 °C/min heating rate (b).

other smaller defects at some other point in the heating cycle. Thus, the procedure used here leads to uncertainty in the determination of the failure temperature, as the defects must be sufficiently large for detection while not occurring at a location on a sample hidden from observation. The failure temperature, starting temperature, and threshold pressure were analyzed for the $4 \times 4 \times 4\ cm^3$ cube sample and the results are listed in Table 3.

Table 3
Observed failure temperature and corresponding threshold pressure and starting temperature of the heating cycles.

T_f	°C	160	180	200	220
P_t	(–)	1.25	1.54	2.00	2.56
T_s	°C	159.6	178.8	197.6	212.6

Fig. 9 shows the predicted MTHC under various failure temperatures. The cycle was obtained from Eqs. (7) and (8) with the determined threshold pressure listed in Table 3. For this analysis, the $4 \times 4 \times 4\ cm^3$ cube sample was applied and the kinetic parameter from the heating rate of 1 °C/min was used. Because the failure temperature of the sample was not clearly observed, we analyzed MTHC for the different threshold pressure corresponding to the failure temperature. If the sample failure occurred at 160 °C, then the starting temperature and threshold pressure would be 159.6 °C and 1.25, respectively, as shown in Fig. 10. The MTHC would be 85.4 h. If the failure

occurred at 220 °C, the MTHC would be 9.8 h. The prediction of MTHC shown in Fig. 10 was based on all of the model parameters, along with their associated errors, from the approximated model equations. Because of all of these coupled uncertainties, safety factors can be applied to both time and temperature [7]. During the heating cycle obtained from the variational calculus algorithm, the volume fraction of the pore former and binder, the reaction rate, and the permeability all vary with time and temperature, as shown in Fig. 11. In the early stages of the heating cycle, the rate of temperature increase must be kept sufficiently low to satisfy the constraint on constant P_t, and as the pore former and the binder are removed and more porosity is created, the heating rate can be increased in a continuous manner.

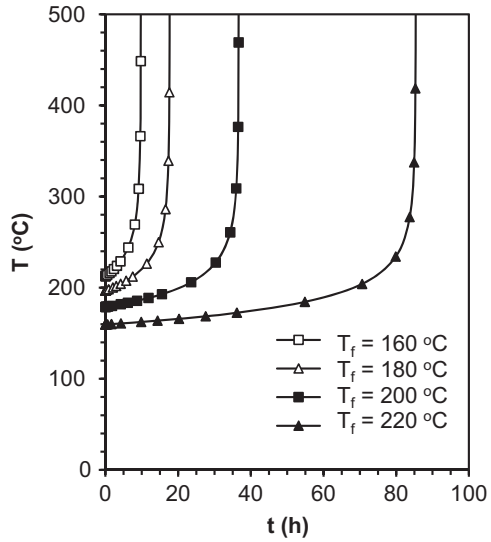

Fig. 10. Temperature profiles with time determined by the variational calculus algorithm for first-order decomposition kinetics at different failure temperatures, T_f.

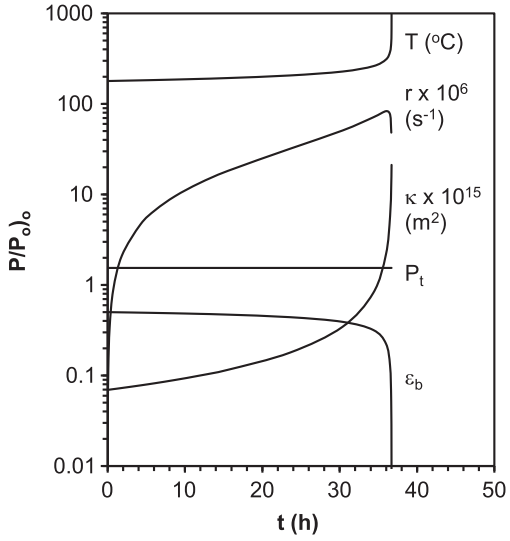

Fig. 11. Temperature, reaction rate volume fraction of pore former and binder, permeability and threshold pressure as a function of time for MTHC at T_f=200 °C.

The process of PMMA pore former removal from honeycomb type anode support is a coupled problem in that reaction kinetics, heat transfer, and mass transfer are interrelated and these processes may lead to sample failure during pore former removal. To reduce the overall problem complexity, we developed MTHC models based on the combination of both experimental and simulation results. The physical parameters such as pore size, porosity, and density can be obtained in experimental methodologies for mass transfer analysis. The kinetic parameters can also be obtained from TGA analysis. Interpretation of the kinetic analysis can be very complicated because multicomponent mixtures such as PMMA, binder, and some additives are decomposed and the catalytic effects of YSZ and Ni are associated. To simplify these difficulties, however, TGA data are interpreted in terms of a single decomposition mechanism, as shown in Table 2. Although it is difficult to use the models to describe the pressure distribution in the honeycomb-type sample bodies, the algorithm from the variational calculus for predicting the MTHC is based on a constraint on pressure build-up within the green body that cannot exceed the threshold pressure. This algorithm is attractive because it provides a clear-cut boundary on the minimum time for the pore former and polymeric binder removal. The predicting model for the MTHC can provide a shortened time with appropriate heating temperature while avoiding any sample defects during the removal of the polymeric binder and pore former.

5. Conclusion

To fabricate anode-supported, honeycomb-type SOFCs without any of the defects that typically occur during thermal pore former removals, MTHC was applied to the honeycomb-type substrate. Experimental measurements and modeling were used to determine a number of parameters appearing in the heating cycles by specifying the decomposition kinetics of the pore former, the permeability, the porosity, the scaling and distribution of the pore former, and other conditions during heat treatment. The results of these measurements and approximations were incorporated into a variational calculus algorithm for predicting the MTHC. The procedure described in this study can be used to develop a rapid heating cycle for a green ceramic and polymer mixture body, including honeycomb-type SOFC anode supports, without producing any defects.

Acknowledgments

This study was financially supported by the Chonnam National University, 2011.

References

[1] B. Zhu, G. Meng, B.E. Mellander, Non-conventional fuel cell system: new concepts and development, Journal of Power Sources 79 (1999) 30–36.

[2] M. Wetzko, A. Belzner, F.J. Rohr, F. Harbach, Solid oxide fuel cell stacks using extruded honeycomb type elements, Journal of Power Sources 83 (1999) 148–155.
[3] H. Zhong, H. Matsumoto, T. Ishihara, A. Toriyama, Honeycomb-type solid oxide fuel cells using $La_{0.9}Sr_{0.1}Ga_{0.8}Mg_{0.2}O_3$ electolyte, Chemistry Letters 36 (7) (2007) 846–847.
[4] T. Yamaguchi, S. Shimizu, T. Suzuki, Y. Fujishiro, M. Awano, Development of honeycomb-type SOFCs accumulated with multi micro-cells, ECS Transaction 7 (1) (2007) 657–662.
[5] T. Yamaguchi, S. Shimizu, T. Suzuki, Y. Fujishiro, M. Awano, Development and evaluation of a cathode-supported SOFC having a honeycomb structure, Electrochemical and Solid-State Letters 11 (7) (2008) B117–B121.
[6] J.W. Yun, S.J. Lombardo, D.S. Krueger, P. Scheuer, Effect of decomposition kinetics and failure criteria on binder removal cycles from three-dimensional porous green bodies, Journal of the American Ceramic Society 89 (1) (2006) 176–183.
[7] J.W. Yun, S.J. Lombardo, Methods for introducing safety factors into minimum time heating cycles for binder removal from green ceramic bodies, Journal of Ceramic Processing Research 8 (6) (2007) 402–410.
[8] J.W. Yun, S.J. Lombardo, Determination of rapid heating cycles for binder removal from open pore green ceramic components, Advances in Applied Ceramics 108 (2) (2009) 92–101.
[9] T.V. Lee, S.R. Beck, A new integral approximation formula for kinetic analysis of nonisothermal TGA data, AIChE Journal 30 (1984) 517–519.
[10] L.C.K. Liau, B. Peters, D.S. Krueger, A. Gordon, D.S. Viswanath, S. J. Lombardo, Role of length scale on pressure increase and yield of poly (vinyl butyral)-barium titanate- platinum multilayer ceramic capacitors during binder burnout, Journal of the American Ceramic Society 83 (11) (2000) 2645–2653.
[11] S.J. Lombardo, Z.C. Feng, Analytic method for the minimum time for binder removal from three-dimensional porous green bodies, Journal of Materials Research 18 (11) (2003) 2717–2723.